Radiometric Correction of Laser Scanning Intensity Data Applied For Terrestrial Laser Scanning.

Nathan Sanchiz-Viel, Estelle Bretagne, El Mustapha Mouaddib, Pascal Dassonvalle

Radiometric Correction of Laser Scanning Intensity Data Applied For Terrestrial Laser Scanning

Nathan Sanchiz-Viel[a,*], Estelle Bretagne[a], El Mustapha Mouaddib[a], Pascal Dassonvalle[b]

[a] *Laboratoire Modélisation, Information et Systèmes (MIS), Université de Picardie Jules Verne (UPJV), 14 quai de la Somme, 80000 Amiens, France*
[b] *ESIEE-Amiens, 14 Quai de la Somme, CS 10100, 80082 Amiens cedex 2, France*

Abstract

Alongside spatial information, an intensity scalar is also measured by LiDAR (Light Detection And Ranging) sensor systems. It corresponds to the amplitude of the backscattered laser beam after reflection on the scanned surface. This information isn't directly usable due to dependencies of geometrical parameters occurring during the scanning process and additional processing modifications. The research community, in a growing trend, invests efforts to convert this signal into a value which could bring qualitative and quantitative new applications. We propose in this paper, a review of the theorical background of LiDAR radiometric calibration, from physical background to state-of-art methodology. A comparison of two approaches to eliminate geometrical (range and incidence angle) and instrumental dependencies of intensity measurement is presented. Their application on several homogeneous areas of a real-world case study shows a significant reduction of intensity variation between surfaces with identical material composition. Finally, a linearization process permits to obtain an equivalent Lambertian reflectance value which, by its disciminant potential, could be specifically suitable for some algorithms like segmentation or registration.

Keywords: LiDAR, TLS, radiometric correction, intensity, reflectance

1. Introduction

1.1. Background

LiDAR is a high-end technology to rapidly and efficiently record depth information and therefore 3D geometry of an object or a landscape. Since few decades, this technique has become more and more popular and is currently used in a large variety of domains: land and building surveying, ecological monitoring, autonomous car navigation, heritage preservation, just to name a few. These fields of applications are the object of increasing interest in research nowadays [13, 12]. During acquisition, a distance map - named

*Corresponding author:
Email address: nathan.sanchiz@u-picardie.fr (Nathan Sanchiz-Viel)

point cloud - is generated by a laser round-trip process on a quasi-spherical Field Of View (FOV), without any contact with surrounding environment. It also provides an additional attribute, inaccurately called intensity, mostly a function of the laser beam measured power after reflection on a surface.

In this article, we limit our study to monochromatic LiDAR applied for Terrestrial Laser Scanning (TLS) technique, whose range is typically from less than 1 meter to about 150 meters. A commercial monostatic TLS sensor is composed of several parts: the laser range unit (laser emitter and receiver, internal signal processing), the scanning unit (oscillating strip-wise mirror), and the integrating instruments unit (GNSS, GPS, altimeter). Generally, terrestrial scanners are also equipped with a digital camera and are able to extract RGB color values from photography in order to match a color to each point [10].

Recorded intensity is based on a measure of the electronic signal strength which is obtained by converting and amplifying the backscattered optical power of the emitted signal. Intensity measurement is, first and foremost, a means of controlling the quality of range information. Indeed, the scanner detector is originally not designed for intensity measurement, but rather to optimize the range determination. Range-related error could be associated with too-low intensity value [1]. That's why most of LiDAR manufacturers add intensity modifiers to the measurement process. Particularly, a too-low signal amplifier, an automatic gain control, and a near distance brightness reducer have been reported for some LiDAR models [32, 29, 17, 9]. The existence of these internal processings is almost never specified, leading intensity measurement to an undocumented, non-standardized and sensor-model dependent value.

While spatial information is directly available for use, that is directly converted from spherical to Cartesian coordinates, the given intensity needs a pre-processing step before being practically usable. The dependence of geometrical parameters and non-linear internal signal processing make the intensity information vary strongly for an homogeneous surface, especially at low distance. This fact is also particularly noticeable for two scans of a same surface scanned from two different positions. A radiometric correction allowing physical interpretation of the intensity would permit to take advantage of this by-product LiDAR recording signal.

The reflectance, or reflection factor, corresponds to the proportion of illuminator beam reflected (optical power) by a material surface. At the operating laser wavelength, it is an intrinsic characteristic of the target surface depending on various parameters, e.g., surface color, material properties. Since emitted beam power is theoretically not varying with time, the received radiant power after reflection could be considered at first sight as an analogue of this singular value. But raw intensity and reflectance are neither equal nor proportional. Potential sources of signal alteration and disturbance can vary in both nature and amplitude, and are complex to quantify accurately. Most of them are systematic, such as optical instrumentation and electronics, but some depend on the geometrical parameters of measurement.

According to the literature [27, 34, 24], the two most important variables to consider are distance, i.e. Cartesian distance between targeted surface and scanner origin, and angle

of incidence, i.e. the angle between the laser beam and the normal to the scanned surface. All of these intensity modifying effects are blended in the resulting data, e.g., fluctuation with distance is caused by natural spreading loss but also by scanner electronics.

The objective of the radiometric correction is to convert the intensity values into parameters related to the surface characteristics. An absolute reflectance can only be extracted with a total control of all phenomena affecting the intensity amplitude. As a black-box system, LiDAR scanner does not permit to have an accurate knowledge of its internal variables, e.g. laser emiter and receiver temperature, and only allows to obtain a corrected intensity or a pseudo-reflectance, that is, an increasing function depending on reflectance.

1.2. Motivation & Objectives

A review of LiDAR radiometric correction was proposed by Kashani *et al.* [32]. They exposed the basic principles of LiDAR intensity measurement, a normalized terminology and a notation framework, which are partly used in this document. Scaioni *et al.* [42] presented a survey of LiDAR intensity applications, and showed its pertinence in a large diversity of fields such as land classification, geology, ecology and building surveying. For example, Errington *et al.* [16] used LiDAR intensity data for clay mapping, Gonzalez *et al.* [2] applied TLS intensity data to damage detection for historical buildings. It appears that most of the studies use either uncorrected intensity, basic correction method or inter-scan normalization approach.

A corrected intensity could be of major interest for some specific algorithms in need of discriminant information, e.g., segmentation, clustering, registration. We thought that a study focusing directly on TLS applications, with details on some correction models, could enhance future research that might find improvements with more advanced radiometric correction models.

In this paper we outline the parameters induced in LiDAR intensity measurement, we summarize and compare a state-of-the-art correction method with a more general and practical approach, and we finally propose a mean to convert the obtained viewpoint-independent corrected intensity into a value related to the material reflectance.

1.3. Structure

The second section exposes the physical background of TLS intensity measurement, taking into account the different sources of signal modification. The third section analyzes the radiometric correction issue and proposes a brief review of literature methods. Section 4 is dedicated to experimental results. Finally, we conclude about radiometric correction in section 5.

2. Physical quantities involved: optical power and reflectance

2.1. Reflectance

During a scanning process an illuminator beam enters the region containing the target wherein an interaction takes place, giving rise to a reflected beam. With laser-based remote sensing, the backscattered laser radiation is only measured in one direction instead

of the entire hemisphere of reflected light, i.e. the received power is a directional portion of the entire reflected power. The more precise decomposition of this phenomenon is the Bidirectional Reflection Distribution Factor (BRDF) representation:

$$BRDF = \frac{\text{differential radiance}}{\text{differential irradiance}} \tag{1}$$

The reflectance ρ is defined as the ratio of reflected radiant flux (optical power) to the incident flux at a reflecting object for a given incident radiation (spectral composition, polarization and geometrical distribution), and is obtained by integration of the BRDF. Various definitions arise depending on the directionality of the radiations being considered (Figure 1). In the case of the TLS we can best talk about biconical reflectance, or directional-conical reflectance if the laser beam is considered infinitely thin with no lateral extension.

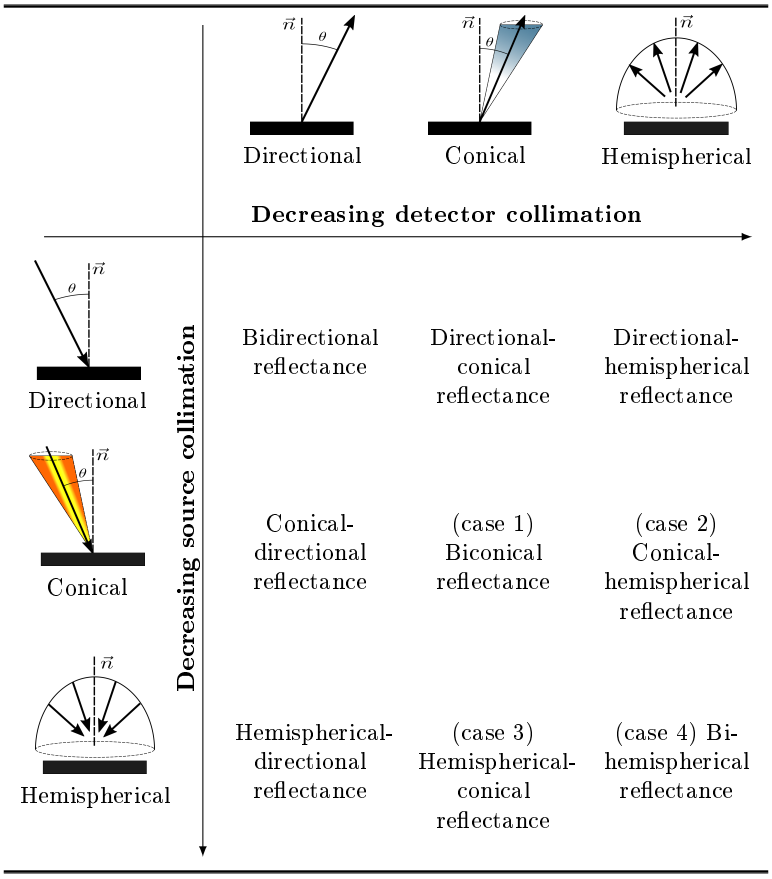

Figure 1: Nomenclature of Nicodemus *et al.* [35]. Cases 1 to 4 correspond to measurable quantities, the others denote quantities that can't be measured directly.

A Lambertian surface reflects radiance equally into all directions. Its BRDF is equal to

ρ_L/π, where ρ_L is the reflectance of the surface under lambertian assumption. Thus the reflectance of a Lambertian surface depends neither on the direction of incidence nor on the viewpoint of the receiver.

The BRDF is a ratio of infinitesimal quantities, therefore it is a derivative with instantaneous values that can't be measured directly. All measurable quantities of BRDF are performed with conical or hemispherical solid angles of observation and illumination. Likewise the reflectance values are average values over the illuminated surface.

2.2. LiDAR target-beam interaction

We denote the power ϕ_r (in watt) of the signal received by the detector. R is the range between the sensor and the target, α is the incident angle between the laser beam and the normal direction of target area. Table 1 resumes the notations used in this paper.
The monostatic directional-conical case was studied in a previous work from a purely optical point of view [6], with the following assumptions:

- The laser beam can be considered as infinitely thin without any lateral extension.
- The point M represents the point of incidence on the target.
- The laser beam emits the power ϕ_i that is completely intercepted by the target.
- Every point on the target is considered to be a flat Lambertian reflector.

The entrance surface of the light receiver is a disk with a diameter D (receiver aperture diameter). If the target is not smooth enough, the multiple scattering from M by neighboring points around M will cause a change in value of the elementary power applied on the receiver by M. Let η_{rough} be the coefficient linked to this phenomenon. After calculation, the received signal power ϕ_r is:

$$\phi_r = \frac{2\,\eta_{sys}\,\eta_{atm}\,\eta_{rough}\,\eta\,\phi_i}{3}\cos^2(\alpha)\,\left(1-\cos^3\theta_{max}\right) \tag{2}$$

where $\theta_{max} = \arctan(D/2R)$, η_{sys} is the system transmission factor, η_{atm} the atmospheric transmission factor, and $(1-\eta)$ represents the absorption coefficient at the considered point for a specific wavelength λ. The demonstration of Equation (2) is not shown here. The interested reader may advantageously refer to the appendix of the reference [6] where the proof is given in great detail.

Laser scanning operates according to the same physical principles as microwave radar, but at a shorter wavelength [20, 22, 41]. According to the radar equation, the LiDAR monostatic case satisfies:

$$\phi_r(t) = \phi_i(t-\frac{2R}{c})\,\frac{D^2}{4\pi R^4\beta^2}\,\eta_{sys}\,\eta_{atm}\,\sigma \tag{3}$$

where β is the laser beam width, and σ the effective target cross-section defined by $\sigma = 4\pi\int_S BRDF(\alpha)\cos^2\alpha dS$ with α the laser incidence angle of the facet dS. There is usually no analytical σ expression in the case of a complex target. For the sake of simplicity, we do not detail the calculations related to the concept of target cross section. The interested reader may refer to the reference [35] or more recently to the reference [51] which exposed the scattering theory. Moreover the simple equation (3) does not predict

Symbols	
λ	Wavelength (m)
ϕ	Light flux (W)
α	Incident angle between the laser beam and the target area normal (rad)
R	Range between the sensor and the target (m)
I	Measure of electronic signal strength which is obtained by converting and amplifying the backscattered optical power of emitted signal
ρ	Reflectance (dimensionless)
τ	Surface roughness (dimensionless)
β	Laser beam width (m)
η_{sys}	System transmission factor (dimensionless)
η_{rough}	Coefficient linked to multiple scattering (dimensionless)
η_{atm}	Atmospheric transmission factor (dimensionless)
$(1-\eta)$	Absorption coefficient of the target for the specific wavelength (dimensionless)
σ	Effective target cross-section (m^2)
D	Receiver aperture diameter (m)
θ	Laser beam divergence (rad)
$BRDF$	Bidirectional Reflection Distribution Factor (dimensionless)
BRF	Bidirectional Reflectance-distribution Factor (dimensionless)
Sub- and superscripts	
i	Incident
r	Reflected
L	Under Lambertian assumption
raw	Relative to uncorrected raw intensity
cal	Relative to a calibration target
cor	Relative to corrected intensity

Table 1: Notations used for the monostatic LiDAR target-beam interaction

the behavior of radar equipment with accuracy.

Equation (3) is equivalent under Lambertian and extended target assumptions to the simplified monostatic radar equation that is applicable to LiDAR [22]:

$$\phi_r = \phi_i \, \rho_L \, \eta_{sys} \, \eta_{atm} \, \frac{D^2 \cos \alpha}{4R^2} \tag{4}$$

The interested reader will advantageously refer to references [20, 22] for more details on how to obtain well-known equations (3) and (4). Here the effective cross-section of the target (backscattering cross-section) is determined by assuming that the target area is circular and scattering solid angle of target is π steradians. Equation (4) represents only the average return power from a simplified target model [44].

Steinvall [44] studies the effects of target shape on laser radar cross section: the problem is to physically define the exact part of the reflecting surface entering into a measurement, i.e., the target effective cross section σ. Equation (4) represents only the average return power from a simplified target model [44]. Shapiro [43] proposes a more complex conceptual framework for target-beam interaction where the target is characterized by a two-frequency bistatic scattering-amplitude matrix.

Concerning the atmospheric factor, for horizontal propagation, the attenuation range is about 0.2 dB/km for extremely clear conditions and 3.9 dB/km for haze conditions [22]. That is, the atmospheric attenuation varies from 0.995 to 0.914 for an object measured at 50 meters. In TLS, under clear atmospheric conditions and limited ranges, η_{atm} can therefore be assumed to be constant or even neglected.

2.3. Reflecting surface characteristic

The light reflection is strongly wavelength dependent: biochemical composition, color or material absorbance do not act identically at different frequencies. For example, at equal energy, the higher the frequency is, the less the wave penetrates through a material, but the more it will be sensitive to humidity [52]. Due to their light absorbance and re-emittance diffusion, translucent surface might also produce noise in backscattered beam intensity. Godin *et al.* [19] have conducted a study on marble surfaces but specifically about geometrical errors.

In most of the studies, for a simpler approach, surfaces are considered as perfect Lambertian reflectors. But for real world materials such assumption becomes rapidly invalid if their surfaces contain non-negligeable specular reflection proportion or wetness. Diffusivity and specularity are naturally distributed in all surface reflection spectrum. An highly diffuse surface could be described by the Lambert's cosine law; a mirror-like surface by the Snell–Descartes law. Over time, material reflectance can vary. For example grain size and temperature of snow affect the intensity amplitude [28].

A surface that obeys Lambert's Law appears equally bright from all viewing directions, but the light optical intensity follows a cosine reduction rule in function of the angle of incidence α. A large number of real-world surfaces, such as concrete, plaster or sand, could be considered almost Lambertian. More generally, light that is reflected on a non-metallic and/or on a very rough surface gives rise to a diffuse reflection.

At contrary, light that is reflected on a relatively smooth surface, gives rise to a specular reflection. Several models were developed in an effort to modelize or approximate natural light behavior: e.g., Phong [40], Blinn-Phong [5], Cook-Torrance [49]. This kind of reflection is especially predominant for metal surfaces. Consequently, the higher the portion of non-Lambertian reflectance properties (specular scattering), the smaller the amount of light backscattered to the sensor if the beam angle of incidence differs from normal incidence. Ding *et al.* [11] have presented a filter to reduce specular influence for intensity correction using Phong reflection model, describing surface reflection as a combination of specular and diffuse components.

Several studies were conducted to take into account material rugosity. For quantifying the roughness factor of a scanned surface, Carrea *et al.* [8] have developed a method based on the Oren-Nayar reflectance model [36], simulating the roughness as a serie of micro-facets acting as perfect diffuse reflectors.

2.4. Intensity measurement

There are commonly two types of LiDAR laser measurement systems: pulsed, commonly called Time-of-Flight (ToF); and Continuous-Wave (CW). The former technique consists in the comparison of the time difference between a pulsed light beam emission and the returned peak energy. For the latter, a continuous beam is emitted with frequency modulation (FM), or sometimes amplitude modulation (AM), and distance is retrieved from the shift-phase difference with backscattered signal. This technique allows the determination of more accurate measurements, but the higher computational cost and the lower laser operating power imply a less maximum range capacity.

LiDAR intensity measurement process, with electronics involved and phenomena affecting the signal, is schematized in Figure 2. The backscattered energy power is firstly converted into photocurrent through a photodetector (photodiode, photomultiplier), then reconverted into a voltage and amplified. The resulting signal is finally quantified via an Analog-to-Digital Converter (ADC) into a Digital Number (DN), through an unknown proprietary function.

The energy received by the photodetector generates electrical charge carriers within the semiconductor. This light-induced current is proportional to the intensity of the incident radiation. The output DN information is generally encoded on 8-bits, 12-bits or 16-bits, varying with scanner manufacturer. The use of an ADC implies that the resolution of the measure is determined by the quantification. The resolution determines the magnitude of the quantization error and therefore the radiometric calibration accuracy [9]. For example, on the Faro Focus 3D 120 the smallest recording difference is about 2-bits on a 13-bits [-2048;+2047] DN scale, meaning that the intensity values could take 2048 possible states.

In this process, signal disturbances could arise from a large variety of sources, e.g., electronical and optical noises, temperature, environnement. For example, shot noise and dark current effects are inherent with photodetector electronic. Frequency-modulated Continuous-Wave (FMCW) LiDAR electronics circuitry appears to be more sensible to temperature than ToF one, affecting laser with power stability or beam profile. Errigton

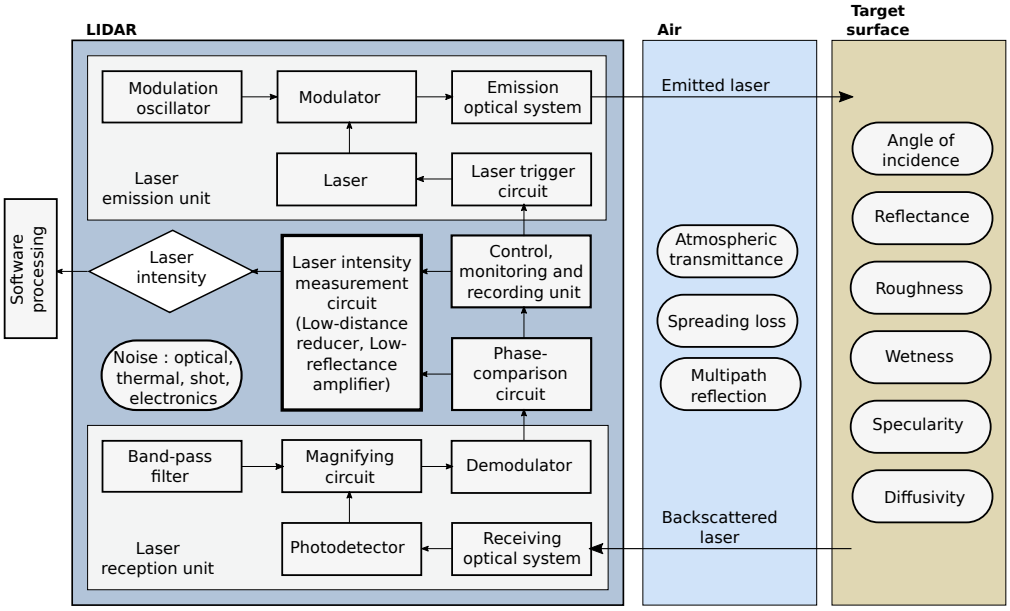

Figure 2: LiDAR FMCW intensity measurement processes with phenomena affecting the backscattered signal. Squares represent the signal processing steps and rounded squares the different sources of signal modifier.

et al. [14] have compared the intensity measurement with varying LiDAR temperature from 5° to 40° and have shown a significant deviation. Also, in normal condition of use, the environment is not entirely controlled and multi-path light reflection (wiggling), scattering particles or mutual interference of the received beam (speckle) could occur.

Beside, intensity outlier can occur due to partial or specular reflector, non-reliable normal estimation, or due to a measure overlapping two distant surfaces. At the time of data processing, constraints can be introduced to minimize these influences such as giving a reduced weight for too-hard incidence angles or ignore the values outside an accepted homogeneity criterion. Actually it is hard to say which perturbation source reaches significant magnitude without dedicated experience in totally controlled environment.

Since acquisition of both range and intensity is based on a monochromatic pulsed laser, the measured intensity value is almost completely insensitive to global or local illuminations from other light sources, thus avoiding the over and under-exposition issues [6]. Finally, it has to be noticed that some proprietary softwares may apply further intensity scaling or unpredictable data modifications during the raw file processing, as a gamma correction [6, 29], without any detailed notification.

3. Radiometric correction

The objective behind radiometric correction is to find a sequence of corrections to convert the raw intensity into a value proportional to the surface reflectance at each scanned

point. It is necessary to develop methods to significantly reduce the different effects influencing the raw intensity measurement. The more obvious are geometrical parameters (range and incidence angle), but temperature and specularity are others one which could be quantified, but with more difficulties.

Typically, the calibration of an instrument is performed by checking its response to several points throughout a certain range, called calibration range. The calibration range is different from the instrument capacity range. Obviously this would change according to needs and signal to noise ratio. Since the manufacturer intensity recording system is not documented and in absence of additional data, all we can do is establish assumptions according to intensity measured behavior.

In this context, correction of both distance and angle of incidence effects allows to convert the recorded raw intensity into a viewpoint-independent information, as if all points were measured at the same distance orthogonally to the scanner. It is therefore possible that in the future, radiometric calibration will be directly introduced inside the LiDAR signal processing unit, which will give directly the true or relative reflectance value. That is partly already the case for Riegl V-line LiDAR which provides range-calibrated pseudo-reflectance using a look-up table as reference [39].

The literature proposes several correction methods which could be divided into two groups: model-driven and data-driven. No general law could be established regarding the variation of measurement behavior between scanner models [33]. Some studies focus their correction on a specific part of intensity measurement, e.g., brightness reducer [17], surface roughness influence [53], incidence angle [18], or a limited portion of range measurement [48, 3]. Table 2 expresses different methods of the literature for both groups.

3.1. Model-driven models

As LiDAR is basically a radar-type system operating with light frequencies, model-driven methods are based on the hypothesis that intensity measurement follows roughly the simplified radar equation (Equation (4)). Considering the reflectance value as the value of interest, Equation (4) could be formulated for a Lambertian surface by:

$$\rho_L \propto \phi_r(\rho_L, R, \alpha)\frac{R^2}{\cos\alpha} \tag{5}$$

Assuming that the relation between the raw intensity I_{raw} and the backscattered optical power ϕ_r is a relation of proportionality we can write:

$$\rho_L \propto I_{raw}(\rho_L, R, \alpha)\frac{R^2}{\cos\alpha} \tag{6}$$

Therefore, for a first approach, the following correction is used for model-based methods:

$$I_{cor}(\rho) = I_{raw}(\rho, R, \alpha)\frac{R^2}{\cos\alpha} \tag{7}$$

This type of model-based approach is based on the following assumptions:

Correction type	Authors	Correction	Equation	Scanner	Measures (increment)	Target
Model-Driven	[8]	R, α, τ	$I_{cor} = \frac{I_{raw}.R^2}{\cos\alpha(A(\tau)+B(\tau)\sin\alpha\tan\alpha)}$	Optech ILRIS-3D^{ER} Optech ILRIS-LR	5-35 m (5 m) 0-80° (10°)	White matte paper
	[29, 30, 26, 27, 50, 31]	R, α, τ	$I_{cor} = 10^{(\frac{I_{raw}}{I_{ref}} - A)/B}$	Faro LS HE80 Leica HDS6000 Sick LMS151	1-30 m (0.5 m) 0-80° (1°)	Spectralon tarp natural materials
Data-Driven	[4]	R	$I_{cor} = I_{raw}(R) + (I_{raw}(0) - F(R))$	Z+F Imager 5006i Riegl LMS-Z420	2-38 m (1 m) 2-50 m (1 m)	Spectralon White panel
	[3]	R, α	$I_{cal}(\rho_L, R, \alpha) = F(R)G(\rho_L, \cos\alpha)$	Faro LS880	0.35-10 m 0-90°	Spectralon various matte surfaces leaf
	[6]	R, α	$I_{cal}(R,\alpha) = \left[1805.4 - \frac{3075.8}{R}\right]\cos\alpha + 1473.9 - \frac{1510.5}{R} + I_{min}$	Leica ScanStation C10	1-23 m (2 m) 0-90°	Sphere
	[15]	R, α	$I_{cal}(\rho_L, R, \alpha) = F(\rho_L, \alpha, G(R))$	Riegl VZ-400 Faro Focus3D	5-89 m 0-80°	Spectralon
	[17]	R, α	$I_{cor} = \frac{I_{raw}}{F_2(\alpha)F_3(R)}$ with $F_2(\alpha) = h\rho(1 - n + n\cos\alpha)$	Z+F Imager5006i	0.9-9 m (0.1 m) 9-50 m (0.5 m) 0-80° (1°)	White panels
	[23]	R, α	$I_{cal}(\rho_L, R, \alpha) = I_{cal1}(\rho_L)F_2(\cos\alpha)F_3(R)$	Leica HDS6100	0-20 m (2 m) 0-60° (10°) 60-80° (5°)	Sand
	[37, 20, 38]	R, α	Separation: $I_{cal} = F(R)G(\rho_L, \cos\alpha)$ Nested: $I_{cal} = F(\rho_L, \alpha, G(R))$ Surface fitting: $I_{cal} = F(\rho_L, \alpha, R)$	Riegl LMS-Z420i Optech ILRIS 3D°	1-15 m (1 m) 15-50 m (5 m) 0-72° (9°)	Spectralon
	[45, 47]	R, α	$I_{cal}(\rho_L, R, \alpha) = I_{cal1}(\rho_L)F_2(\cos\alpha)F_3(R)$	Faro Focus 3D X330	1-29 m(2 m) 0-80° (5°)	Spectralon
	[53]	R, α, τ	$I_{cal}(\rho_L, R, \alpha) = I_{cal1}(\rho_L)F_2(\alpha)F_3(R)$ with $F_2(\alpha) = 10\log(\cos\alpha(A + B\sin\alpha\tan\alpha))$	Riegl VZ-400i	5-12 m (0.3 m) 12-50 m (1.2 m) 0-72° (9°)	Teflon material

Table 2: Table of some representative model-driven and data-driven correction methods. A variety of equations, targets, and experimental measures can be found. The corrections focus on distance (R [m]), incidence angle (α [°]), and surface roughness (τ [dimensionless]).

- No LiDAR electronic modification of the signal.
- No temperature effect.
- Electronic gains of emission and reception remain constant.
- Range effect only depends of spreading loss, and angle of incidence of Lambert's cosine law.
- The effects of range and angle of incidence are independent of each other.
- The reflector is assumed to be an extended Lambertian reflector.

This theoretical model permits a first understanding of the radiometric correction problem, but actual data are inconsistent with the previous hypotheses. A simple law in '$1/R^2$' is not applicable on the whole range of experimental distance behavior [17, 37]. Kaasalainen *et al.* [27] found that the range effect is strongly dominated by instrumental factors. Another limitation of theoretical models is that they do not adapt to all materials but are usually limited to the Lambertian borderline case or to a single type of material.

Other existing models are either a modified version of the simplified radar equation or only limited to a particular category of materials [32]. For example, Carrea *et al.* [8] use Oren-Nayar reflectance model to take into account a lithological relief with micro-facets.

3.2. Empirical / Data-driven models

In the model-driven methods, it has been shown that a number of unknown parameters may exist, and that the actual data are not consistent with the previously listed assumptions. Data-driven methods, based on quantified observations of the intensity measurement behavior instead of a purely theoretical model, are naturally more adaptative and suitable for an adequat correction approach.

3.2.1. Principle

The objective of empirical methods is to modelize the baseline intensity signal of a calibration target with varying parameters in order to determine correction coefficients. The calibration target is often a Lambertian-like flat board such as Spectralon coating panel [21, 45, 15] or white cardboard [8, 17, 4], but some studies used natural or urban objects [7, 9, 48]. Bretagne *et al.* [6] used a spherical target to collect data for all angles of incidence for each range.

Let's consider a 3-D scan of any scene. We want to make the intensity viewpoint-independant by corrected range and incidence angle. For each point of the cloud, the intensity of a calibration target measured at the same range and incident angle could provide a point of comparison. This type of data-driven approach is based on the following assumptions:

- The measures for the calibration target and the scanned scene are made with the same LiDAR.
- All signal changes (e.g. target's surface reflection properties, temperature, atmospheric condition) are of the same order for the considered scanned point and for the calibration target.
- The reflectance of the calibration target is assumed to be fully known or uniform at any point on its surface.

The corrected intensity is therefore defined as:

$$I_{cor}(\rho) = \delta \, \frac{I_{raw}(\rho, R, \alpha)}{I_{cal}(R, \alpha)} \tag{8}$$

where I_{cal} is the raw intensity of the calibration target at both the same range and incident angle. The constant δ is a normalization constant.

This method permits to evaluate the corrected intensities of any material on the basis of the reference behavior, suppressing then the dependence of geometrical parameters. It was the same idea expressed by Nicodemus *et al.* [35]: "*once the absolute reflectances of a set of reference standards are carefully measured, the reflectance measurement of an unknown sample can be more easily done by the comparison method.*". Contrary to the model-driven methods, unknown or unmeasured effects which are hard to modelize correctly could be compensated, and outliers influence reduced.

3.2.2. Interpretation of the corrected intensity

There are various unknown non-linearities between the raw intensity and the optical flux received by the detector. The best we can generally assume for all 3D scanners is that:

- For constant R and α, the function $\rho \mapsto I_{raw}(\rho, R, \alpha)$ which at ρ associates the raw intensity is strictly increasing.
- The corrected intensity superior (inferior) to the constant normalization δ implies that the reflectance is superior (inferior) to the calibration reflectance, respectively.
- With the corrected intensity, the effects of range and angle of incidence are attenuated compared to those present in the raw intensity.

In the end, the corrected intensity approaches a non-linear increasing function of the reflectance only. The corrected intensity is sometimes referred to as relative pseudo-reflectance values or pseudo-reflectance.

A reverse engineering approach can be implemented by using various known reflectance targets in order to identify and correct the non-linear relationship between the corrected intensity and the reflectance, at each point. This data-driven work can be done either directly on the corrected intensity, or upstream on the raw intensity. For example Kaasalainen *et al.* [30] studied the effect of a logarithmic amplifier for small reflectances, and they corrected them by an exponential function fitted on the measures. However, this process must be repeated and adapted for each LiDAR model, and the results should be considered as an equivalent Lambertian reflectance if only a Lambertian target is used. We will present further in this article such a linearization approach in the experimental part.

Thus some authors go back to an estimation of the true or absolute surface reflectance using known reflectance targets. This is called rigorous radiometric correction and calibration [32]. But we must remain cautious about interpreting the results in terms of absolute reflectance. Indeed the measurement conditions are not those used in a standard way for the determination of absolute reflectance. In addition, an average bidirectional reflectance for the illuminated surface is considered here.

3.2.3. Assessment of the raw intensity of a calibration target

A calibration target is scanned at several ranges and several angles of incidence so as to obtain the corresponding raw intensities. Its reflectance is assumed to be fully known or uniform at any point on its surface. Then an extrapolation is made to obtain the raw intensities for the missing ranges and angles of incidence. At the end of the process, the raw intensity I_{cal} of the calibration target is obtained as a function of the range R and the incident angle α.

In the literature, there are several forms for interpolation functions that may or may not be based on the theoretical formulas presented in the subsection *3.1.* Pfeifer *et al.* [38] identified three types of decompositions for data driven calibration intensity. For a Lambertian calibration target with a constant reflectance, these three possible approaches are:

- Separation approach $I_{cal}(\alpha, R) = F(R)\, G(\cos\alpha)$
- Nested approach $I_{cal}(\alpha, R) = F(\cos\alpha, G(R))$
- Surface fitting approach $I_{cal}(\alpha, R) = F(\cos\alpha, R)$

The BRDF of the chosen calibration target should resemble that of the sample as closely as possible to minimize the sensitivity to instrument-alignment errors [35]. The closer the reflectance of the calibration target is to that of the scanned object, the more effective the method is. The ideal would be to have several targets with several reflectances. The closer the measurement conditions for the calibration target are to those used for the scanned object, the better the results. For the sake of accuracy, it is possible to take measurements on the calibration target under the same conditions (place, time, brightness, warm-up time...) as those of the scanned object. In this case the use of a spherical calibration target represents an unquestionable time saving.

3.3. The approaches compared experimentally

In the following subsection two data-driven approaches are presented, and will be compared in the experimental section: a separation approach and a surface fitting approach. The former is usually used in literature, but the latter is more general by not taking into account the hypothesis of variable separability. These two approaches are not specialized for a given range of distances or for a type of material.

3.3.1. A separation approach

Tan *et al.* [45] start from the strong assumption that the effects of Lambertian reflectance, range and cosine of incidence angle on intensity are separable. Their approach consists in the subdivision of the calibration intensity in three sub-functions (separated approach):

$$I_{cal}(R, \alpha) = I_{cal_1}(\rho_L) I_{cal_2}(R, \alpha) \quad \text{with} \quad I_{cal_2}(R, \alpha) = F_2(\cos\alpha) F_3(R) \tag{9}$$

According to the Weierstrass approximation theorem, a continuous function in a closed interval can be approximated by a polynomial series. That is the reason why the functions I_{cal_1}, F_2 and F_3 were assumed to be of the following forms:

$$I_{cal_1}(\rho_L) = \sum_{k=0}^{N_1} \epsilon_k \rho_L^k, \quad F_2(\cos\alpha) = \sum_{k=0}^{N_2} \beta_k (\cos\alpha)^k \quad \text{and} \quad F_3(R) = \sum_{k=0}^{N_3} \gamma_k R^k \tag{10}$$

where N_1, N_2 and N_3 are three integers and all the values ϵ_k, β_k and γ_k are real numbers. According to data observations of distance from 1 to 29 m and angle of incidence from 0 to 80° at 10 m, the authors researched the best polynomial fitting in function of the standard deviation of residual error for each polynomial regression from degree 1 to 10.

Then the corrected intensity is:

$$I_{cor}(\rho) = \delta \, \frac{I_{raw}(\rho, R, \alpha)}{I_{cal}(R, \alpha)} \quad \text{with} \quad \delta = I_{cal}(10, 0) \tag{11}$$

The corrected intensities acquired at other incidence angles and distances were corrected to 0 degree and 10 meters chosen as the standard scanning geometry. Moreover the correction is independent of the reflectance ρ_L of the calibration target:

$$I_{cor}(\rho) = I_{cal}(10, 0)\frac{I_{raw}(\rho, R, \alpha)}{I_{cal}(R, \alpha)} = F_2(\cos 0)F_3(10)\frac{I_{raw}(\rho, R, \alpha)}{F_2(\cos\alpha)\ F_3(R)} \tag{12}$$

Four Lambertian plane targets were used, with Lambertian reflectance ρ_L of 20%, 40%, 60%, and 80% mounted on a board.

3.3.2. A surface fitting approach

To our knowledge, the surface fitting approach has been cited in [38] but not developed. Contrary to the previous method, the assumption about distance and incidence angle separability is not made. Physically, attenuation of laser light beam with distance and incidence angle are two independent phenomena, but the non-linear signal modification of intensity by LiDAR electronic could induce an interdependence effect.

We propose to investigate a surface fitting method to allow the determination of an exhaustive calibration map in the parameter domain. This surface regression is based on a spherical calibration target which is scanned at various ranges, as used by Bretagne *et al.* [6]. Its reflectance is assumed uniform on its entire surface. Hence the only variable parameters are the range R and the cosine of incidence angle $\cos\alpha$: $I_{cal}(R, \alpha) = f(R, \cos\alpha)$.

Spherical geometry contains all angles of incidence, that is specifically convenient for the calibration. The surface fitting is computed by a piecewise bivariate polynomial regression on both range and cosine of angle of incidence. The considered bivariate polynomials are defined on domains that were dependent only on the range R. They are of the following form on each domain:

$$I_{cal}(R, \alpha) = \sum_{k=0}^{M}\sum_{l=0}^{N} \eta_{kl}.R^k.\cos^l\alpha \tag{13}$$

where M and N are integers and the values η_{kl} ($(k, l) \in \mathbb{N} \times \mathbb{N}$) are real numbers. Here, no prior hypothesis is made on the dependence of the effects of distance and incidence angle.

The resulting 3D map provides a piecewise continuous function describing intensity measurement behavior for any point comprised inside the range of measurement of reference target. The corrected intensities acquired at other incidence angles and distances were corrected to 0 degree and 10 meters chosen as the standard scanning geometry.

4. Experimental results

In this section, we present the experimental results of intensity correction obtained with the two previous exposed approaches. Firstly, in order to obtain LiDAR intensity behavior with distance and incidence angle, two series of measurement were conducted with a Spectralon and a sphere target. We describe the scanner, the targets and the protocol used for our experiments, and expose the resulting raw intensity dependency curves. Secondly, both correction approaches were applied directly on the obtained calibration datasets to validate their effectiveness to reduce the dependency of geometrical parameters. In order to assess the stability of the correction approaches, two point clouds of a large scene taken from different viewpoints and with heterogeneous intensities are corrected. Finally, a linearization of the corrected intensity is proposed.

4.1. Material

The laser scanner used to carry out measurements is a commercial monostatic single-echo and continuous-wave Faro Focus 3D 120 (Table 3) operating in near infrared. Point clouds were extracted with the Faro SCENE software. Intensities were scaled in $[0; 1]$ scale for simplicity.

Range	0.6 m - 120 m
Unambiguity interval	153.49 m
Laser power	20 mW
Wavelength	905 nm
Beam divergence	0.19 mrad (0.011°)
Beam diameter at exit	3.0 mm

Table 3: Technical specifications of Faro Focus 3D 120

Spectralon coating material is used as a calibration reference for intensity correction. Its material property exhibits purely diffuse reflection without specular component, so it is a quasi-ideal Lambertian reflector. For our Spectralon target[1] (Figure 3), the reflectance values given by manufacturer for the four parts are: 0.989, 0.572, 0.284 and 0.109 at the laser operating wavelength (905 nm).

A spherical target (Figure 3) was also employed in the same way as [6]. This target presents several practical advantages over Spectralon: low price, high availability, and easier to handle. In addition, all incidence angle could be measured in a single scanning operation. That type of target is initially intended to be used as registration reference, inducing that their sphericity and reflectivity should logically be as high as possible. But their real material composition and reflectance are not known, likewise, their Lambertian property is uncertain. The diameter of the sphere is about 139 mm.

[1] SRT-MS-180 Multi-step: 99, 50, 25 & 12.5%, 18 x 18 inches, AA-00661-000, Labsphere, North Sutton, New Hampshire, USA

Figure 3: Photography of the used targets: Spectralon with 99%, 57%, 28% and 11% reflectivity surfaces, and sphere.

4.2. Geometrical parameter dependancies

The two more important geometrical parameters to correct are distance and incidence angle. To determine the intensity behavior as a function of these parameters, several measurement series were carried out with identical conditions. The measures were made indoor along a long corridor ($\sim$ 50 m), under daylight illumination. The scanner was stationary and only the target was moved orthogonally to the scanner center. In order to avoid the bias due to the scanner temperature, a few unused scans were made before each measurement serie to preheat the scanner.

For Spectralon, two sets of measures have been taken, one to obtain raw intensity response as a function of distance, and the other one to obtain intensity response as a function of incidence angle. For the first serie, measures were made from 1 to 40 m by 1 m increment. For the second serie, the Spectralon target was rotated by steps of 10 degrees, from 0 to 80 degrees, at different distances: 10, 20, 30 and 40 m. Increments were chosen in order to get enough measurements for an appropriate estimation of the curve tendency. As it appears that there is not abrupt variations, a constant increment is sufficient.

For the sphere target, measures were carried out from 1 to 40 m with 0.5 m increment. Points with angle of incidence superior at 80°, which present high discrepancy, were removed. The curve (Figure 4) shows the data obtained with the sphere and Spectralon as a function of distance and incidence angle.

For the determination of incidence angles, in order to get accurate estimations and preventing noise, normals were estimated using plane fitting for Spectralon point clouds and sphere fitting for sphere point clouds. For each Spectralon parts of the second serie, all points were averaged. For each sphere point cloud, all points were vectorized and organized by class of 5° for visibility.

Considering distance measures, for all points with incidence angle inferior to 15°, distance and raw intensity values were averaged for each Spectralon parts of the first serie, and

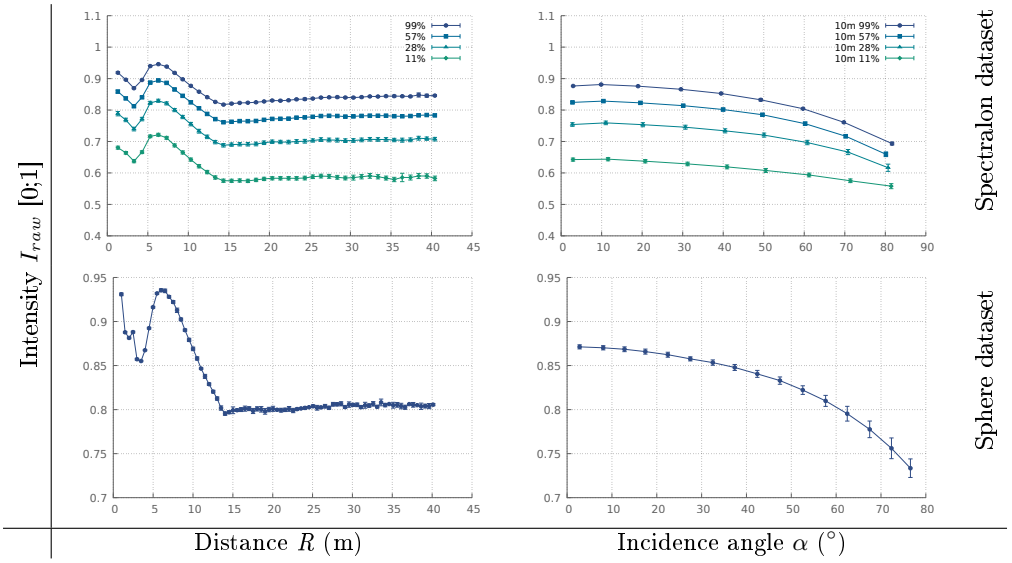

Figure 4: Raw intensities measured of the Spectralon and sphere targets as a function of distance and incidence angle. Left) Mean raw intensities as a function of distance for the four Spectralon parts and sphere target, with a maximal incidence angle of 15°. Right) Mean raw intensities as a function of incidence angle for the four Spectralon parts at 10 m by classes of 10°, and for the sphere target at 10 m by classes of 5°.

for the sphere target. The resulting curves present three separated trends. According to FARO manufacturer, the existence of internal processes modifying the behavior of the intensity measurement is confirmed. At short distance $[0, 6]$ m, a near-distance reducer prevents saturation of the signal. At mid distance $[6, 14]$ m, it seems that the intensity variation corresponds to the unmodified signal measurement. Finally, at long distance $[14, 40]$ m, a too-low signal amplifier heighten the measured intensity to make the values comparable with the near and mid distance values.

This curve shape is very similar to the one obtained previously by Tan *et al.* [46] where the same scanner model, a Faro Focus 3D 120, was used. Along litterature the mid distance behavior generally do not change, at contrary to the short and long distances. For example, with a Faro LS HE80 scanner, Kaasalainen *et al.* [30] have presented a curve with a near distance effect but no modification at long distance. Indentically in [4], with a Z+F Imager 5006i. In [4, 37], where a Riegl LMS-Z420i is used, the near distance effect is not present, and the long distance amplifying effect is smoother than on our data. In [38], an Optech ILRIS 3D is tested and shows a very different combination with a non-stop increasing from 0 m to 20 m and a non-stop decreasing untill 50 m. As these signal modification effects appear alternatively both on ToF and CW LiDAR, it should not be correlated to the type of measurement modality of the scanner.

4.3. Intensity correction

We have strictly followed the method established by Tan *et al.* [45] with the Spectralon dataset. Similar parameter estimations were conducted. Polynomial regression orders

were chosen in regard of the minimal mean error, i.e. $N_2 = 3$ for angle of incidence, and $N_3 = 9$ for distance. The polynomial coefficients (Table 4) were normalized by setting leading term at 1 with a linear process. The normalization constant was chosen on the 28% curve at 10 m, and at an incidence angle of 0°. Graphs of the resulting corrected intensities with this method are shown in Figure 5.

$F_3(R)$	γ_0	γ_1	γ_2	γ_3	γ_4
	-4.918e-12	9.987e-10	-8.615e-08	4.104e-06	-1.174e-4
	γ_5	γ_6	γ_7	γ_8	γ_9
	2.052e-3	-2.121e-2	1.186e-1	-3.031e-1	1
	β_0	β_1	β_2	β_3	
$F_2(\cos\alpha)$	13.196	5.872	-3.277	1	

Table 4: Normalized polynomial coefficients for Separation approach.

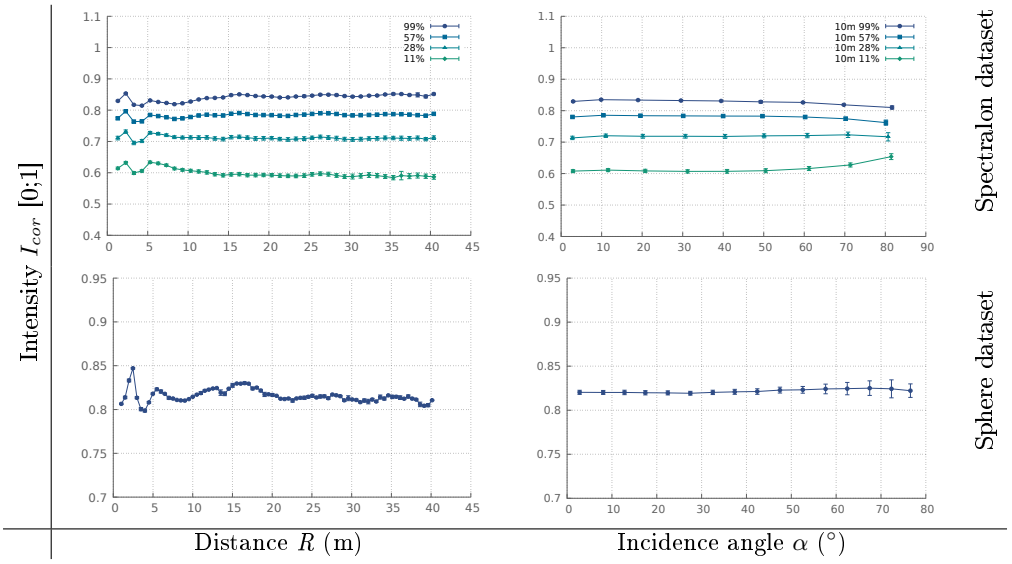

Figure 5: Separation approach applied on the Spectralon and sphere calibration datasets as a function of distance and incidence angle. Left) Mean corrected intensities as a function of distance for the four Spectralon parts and sphere target, with a maximal incidence angle of 15°. Right) Mean corrected intensities as a function of incidence angle for the four Spectralon parts at 10 m by classes of 10°, and for the sphere target at 10 m by classes of 5°.

To evaluate the efficiency of the correction, we will use the coefficient of variation (CV) used in [37, 45, 25], which is a scale invariant and dimensionless quantity, as a statistical quantification of data dispersion. It is defined as the ratio between standard deviation σ and mean μ ($CV = \sigma/\mu$), and is expressed in percentage. Applied on the obtained intensity response curves, this measure is particularly convenient to assess the reduction of intensity variation with regard to parameters.

After application of the correction, intensity variation with distance is reduced from a mean CV of 5.35% to 1.25% with Spectralon dataset, and from a CV of 5.19% to 0.91% with sphere dataset. Intensity variation with incidence angle is reduced from a mean CV of 6.34% to 1.15% with Spectralon dataset, and from a CV of 5.05% to 0.25% with sphere dataset.

Though the scanner used in this study is the same model as in Tan *et al.*, subtle differences of the system characteristics may exist in each individual scanner. Likewise, our experimental environment is not identical. For example, although we also use a Spectralon target, the reflectance values calibrated by the manufacturer are different from those of Tan *et al.*. It is recommended that each TLS should be calibrated individually.

With the surface fitting approach, the regressions of data were segmented in three parts: first segment between 1 and 6 m, second between 6 and 14 m, and third between 14 to 40 m. The regression orders were set to $n = 2$ and $m = 2$. Thus, three second-order bivariate polynomial regressions were applied (Figure 6), one for each distance segment. The normalization factor was chosen at 10 m, for an incidence angle of 0°.

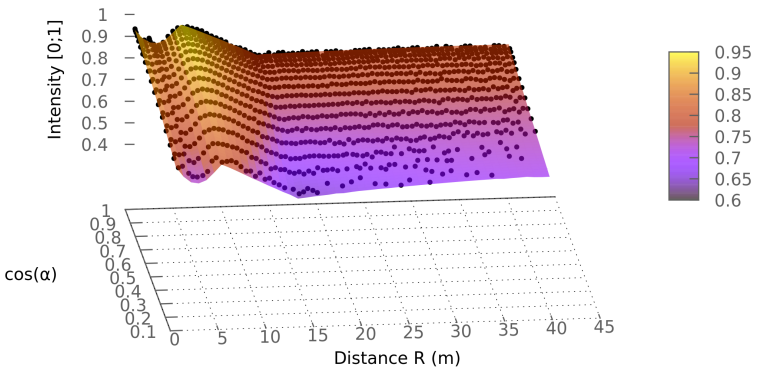

Figure 6: Colored surface regression with raw intensity (black points) as a function of distance and cosine of incidence angle.

The obtained coefficients are presented in Table 5, and the graphs of the resulting corrected intensities with this approach are shown in Figure 7. Intensity variation with distance is reduced from a mean CV of 5.35% to 1.17% with Spectralon dataset, and from a CV of 5.19% to 0.45% with sphere dataset. Intensity variation with incidence angle is reduced from a mean CV of 6.34% to 1.16% with Spectralon dataset, and from a CV of 5.05% to 0.31% with sphere dataset. Quantitative results of both methods are given in appendix (Table 7).

	$F(R, \cos\alpha)$								
R	η_{00}	η_{01}	η_{02}	η_{10}	η_{11}	η_{12}	η_{20}	η_{21}	η_{22}
$(0, 6]$ m	1770.54	-245.11	36.83	308.88	196.60	-25.83	-28.69	-130.92	17.44
$(6, 12.5]$ m	1869.64	-59.66	0.69	366.49	64.23	-2.52	-91.52	-38.15	1.57
$(12.5, 40]$ m	932.36	20.78	-0.20	1415.33	-55.65	0.58	-755.72	38.47	-0.42

Table 5: Bivariate polynomial coefficients for Surface fitting approach.

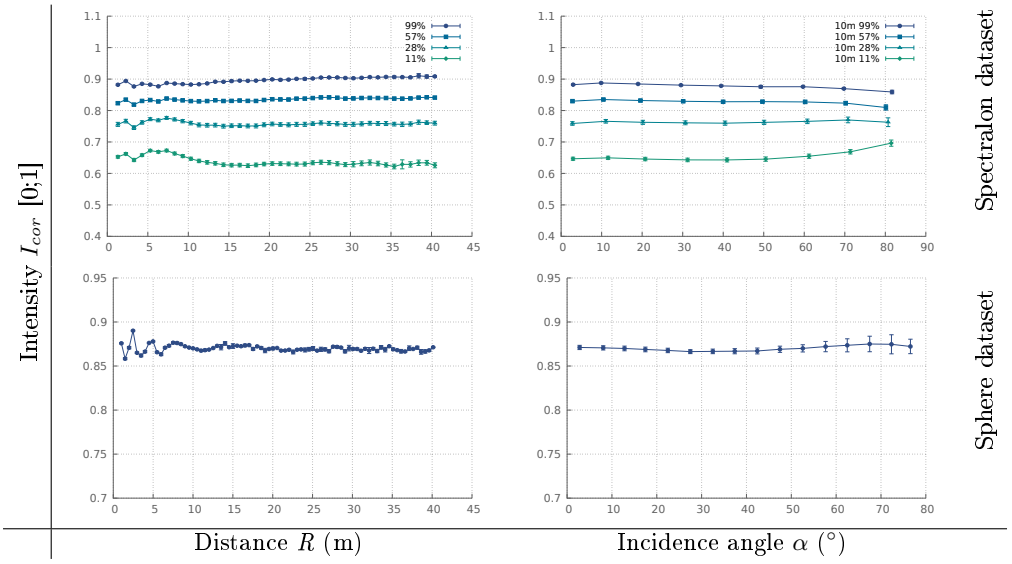

Figure 7: Surface fitting approach applied on the Spectralon and sphere calibration datasets as a function of distance and incidence angle. Left) Mean corrected intensities as a function of distance for the four Spectralon parts and sphere target, with a maximal incidence angle of 15°. Right) Mean corrected intensities as a function of incidence angle for the four Spectralon parts at 10 m by classes of 10°, and for the sphere target at 10 m by classes of 5°.

4.4. Application to a real scene point cloud

We applied the correction methods on a real point cloud scene case, where both distances and incidence angles were diversely distributed in the data. Two scans with different viewpoints of a same place were selected. The scene represents a sculpture of Niki de Saint Phalle, named Arbre-aux-Serpents (Angers, France). As in [46, 17], a mean to assess the correction of an heterogeneous point cloud is to select several areas of a same surface or structure, and compare their degrees of variation before and after correction. Results should state about the homogeneity of the correction on each point clouds whatever the point of view. The point clouds and the selected areas are presented in Figure 8. Both scans were made outdoor under a warm and sunny day.

The selected areas have mean distances which vary from 2.68 m to 37.13 m, and mean incidence angles from 8.39° to 86.68°. Three regions were of interest: ground, sculpture pedestal, and building walls. The predominant material type in all of these regions is formed of white and diffuse stones but with different composition. Ground presents especially variation on distance, pedestal variation on incidence angle, and building walls

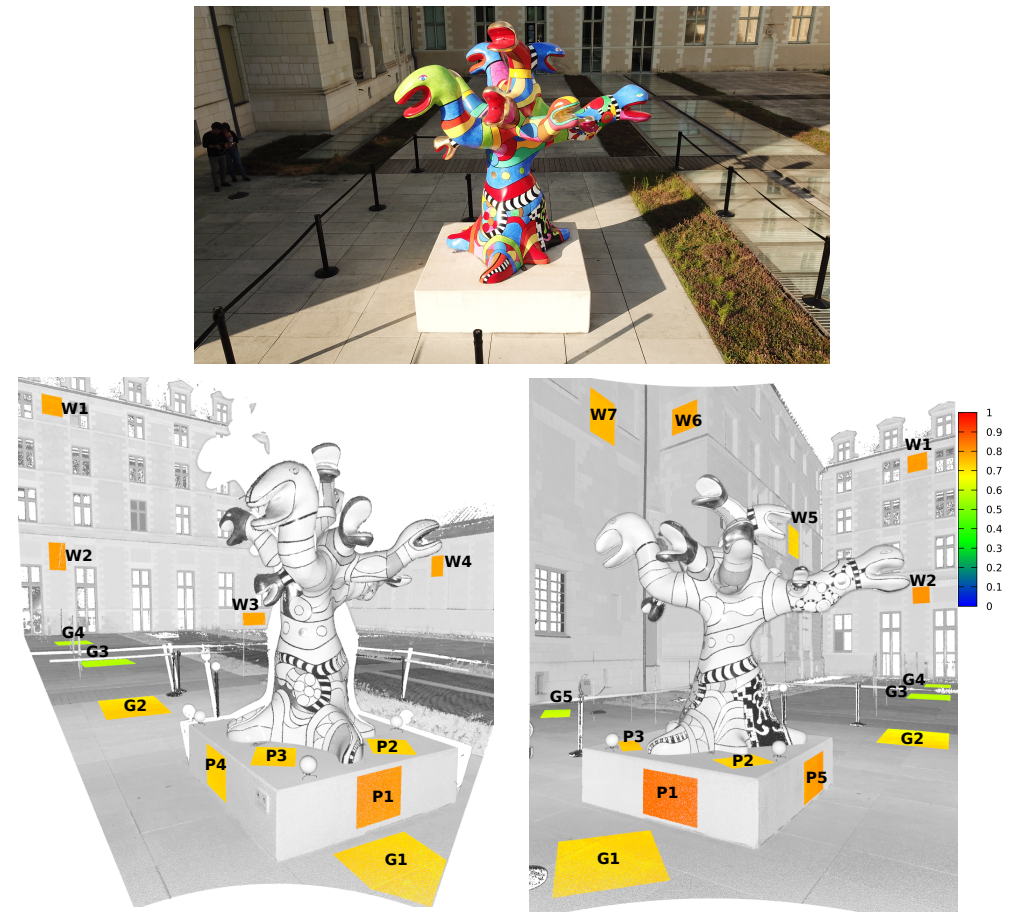

Left side Right side

Figure 8: Top) Front-view photography of the tested scene with heterogeneous reflective materials. Arbre aux Serpents sculpture, Niki de Saint Phalle (Angers, France). Bottom) Point clouds of the sculpture left and right sides (grey tone) with selected areas (false color), dyed in function of the raw intensities.

a mix of both. As the two scans have an overlap, some selected areas are coincident on both point clouds: for the ground region: areas G1, G2, G3 and G4; for the pedestal: areas P1, P2 and P3; for the walls: areas W1 and W2.

Figure 9 presents results of the two correction methods compared with raw intensity. We observe a reduction of intensity variation on the different areas with both methods: areas CV are divided by a factor between 2.67 and 6.58 with Separation approach, and by a factor between 3.84 and 9.56 with Surface fitting approach. Left and right side regions become more homogeneous than before. As the constitutive material of each region is nearly identical, difference between corrected intensities is not very pronounced. Although, we can observe a more significant difference in amplitude between ground and both pedestal and walls.

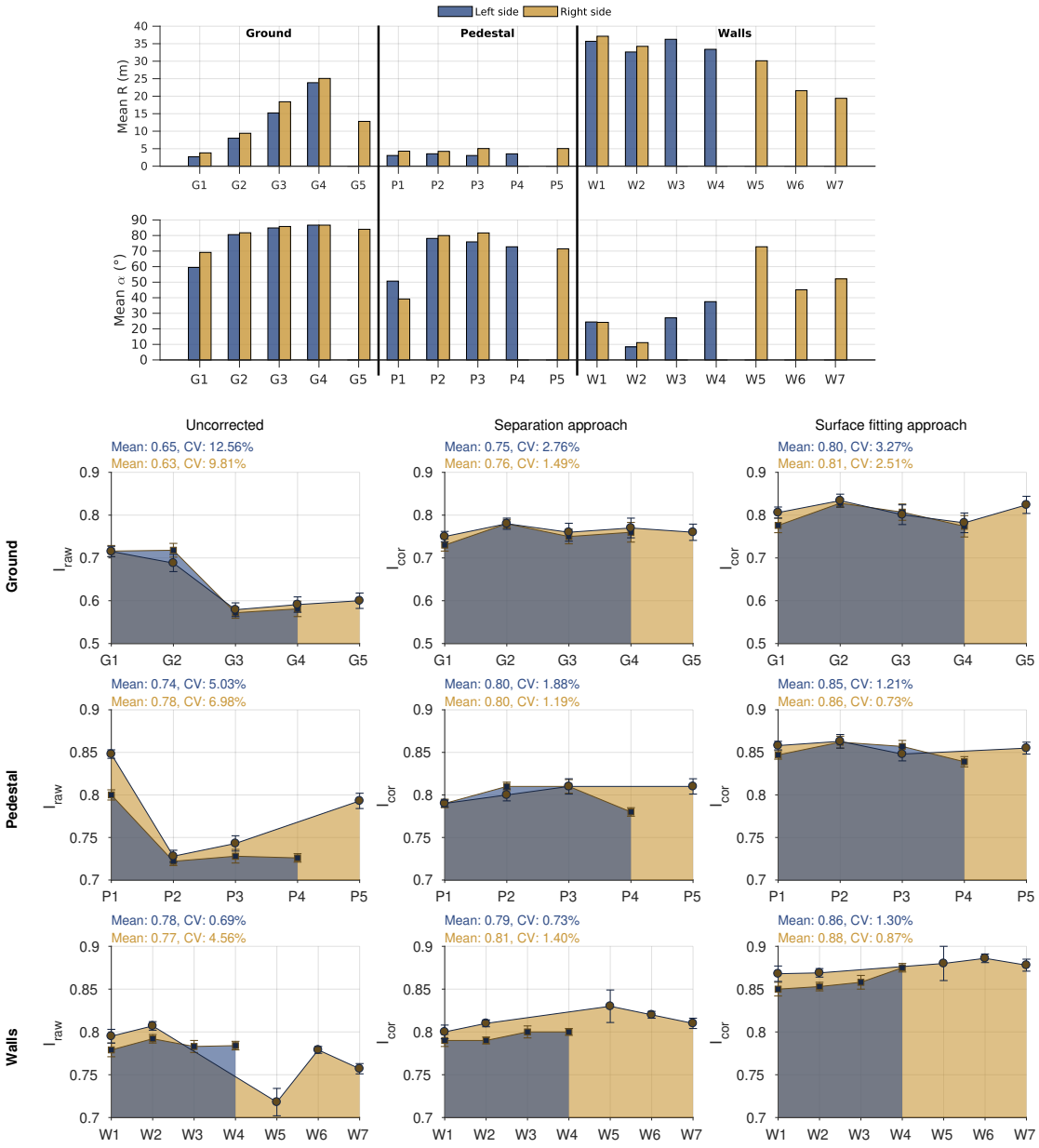

Figure 9: Separation and sphere fitting intensity correction approaches applied on two scans of an heterogeneous point cloud. Top) Selected area mean distances and incidence angles. Bottom) Comparison of area mean intensities before and after correction.

Quantitative results of the area intensities before and after correction are given in appendix (Table 8).

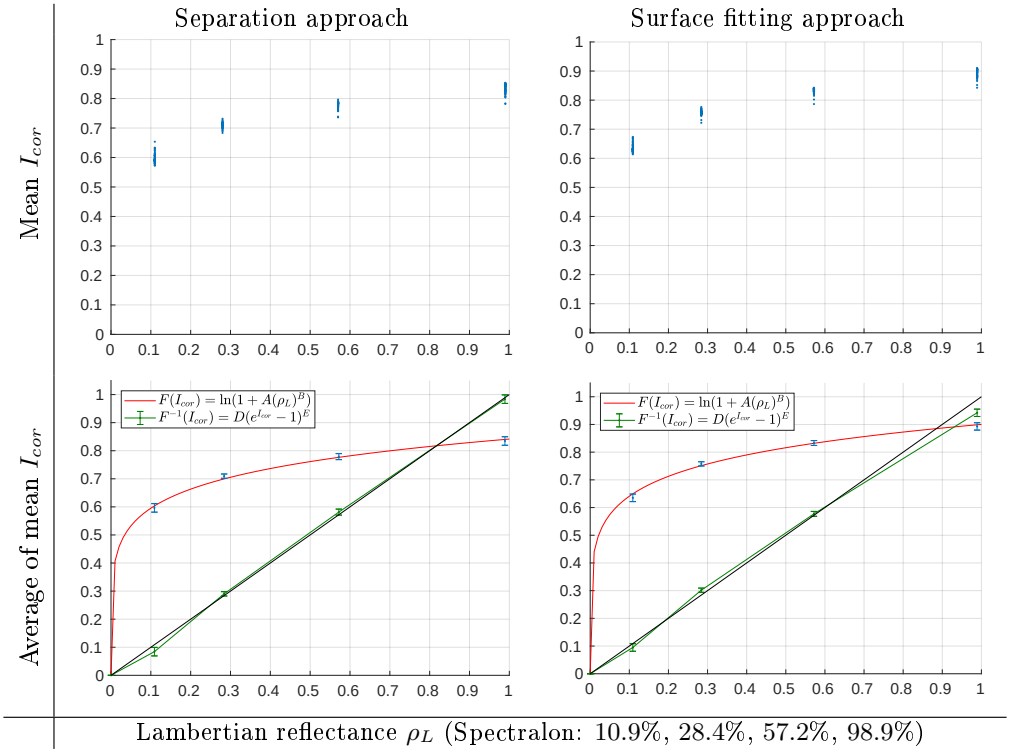

Figure 10: Top) Mean corrected intensities of the four Spectralon parts for various ranges and incident angles. Bottom) Average of mean corrected intensities for each Spectralon part (blue), logarithmic approximation (red curve), and linearized I_{cor} values compared with perfect linear line (black)

The aim of the linearization is to obtain a linear relashionship between the corrected intensity and the Lambertian equivalente reflectance. This linearization is new compared to the method developed by Tan *et al.* [45]. The linearization method used is general and reusable.

288 point clouds with corrected intensities of the four parts of the Spectralon are used to evaluate the non-linear relationship between corrected intensity and Lambertian reflectances for both the separation and the surface fitting approach. Ranges are comprised between 1.30 m and 40.6 m. The angles under consideration are less than 80°. We thus avoid the high dispersion due to the grazing incidence. The coefficient of variation corresponding to the average corrected intensity is always smaller than 4%.

Figure 10 (top) shows that the correction carried out on the raw intensity does not completely eliminate the effects of angle and distance since otherwise the points would be better grouped for a given Lambertian reflectance value. The surface fitting approach makes it possible to better discriminate different Lambertian reflectance values. In both approaches, the accuracy decreases with increasing Lambertian reflectance.

A non-linear relationship between the corrected mean intensity and the Lambertian reflectance is found based on the four mean corrected intensities and the origin. This relationship is approximated by the logarithmic form $F(\rho_L) = \ln(1+A(\rho_L)^B)$ where A and B are constants. Finally, the linearization function is of the form $F^{-1}(I_{cor}) = D(e^{I_{cor}} - 1)^E$. The values of the constants are given in the Table 6.

Constants	Root-mean-square error (RMSE)	A	B	D	E
Surface fitting approach	0.008	1.46	0.21	0.16	4.72
Separation approach	0.006	1.31	0.21	0.24	5.23

Table 6: Constants of linearization for both the separation and the surface fitting approach.

The linearized corrected intensity is an equivalent Lambertian reflectance value since we linearized from four Lambertian targets. Linearization allows us to obtain a more realistic reflectance value with a linear scale but does not fundamentally change the results obtained, since a bijective function is applied. Experimentally the quality of the linearization would depend on the known reflectance targets used to estimate the real reflectance (Lambertian or not). The use of a spherical target to correct the raw intensity and then of a Spectralon to linearize the corrected intensity seems to us from this point of view suitable.

We applied this linearization to the actual scans already presented in the previous section. In Figure 11, in a general way, the regularity of the results is similar for both approaches, with slightly higher equivalent Lambertian reflectance value for the separate method.

For the ground, the separation method gives equivalent Lambertian reflectance mean values between 0.48 and 0.52, whereas the surface fitting approach gives mean values between 0.41 and 0.46. For walls the regularity of the results is similar for both approaches, with very slightly higher equivalent Lambertian reflectance mean values for the separate method. For the pedestal we find the same trend: a very slightly greater range of mean values for the separate approach. Nevertheless the dispersion is a little better for the surface fitting approach in this case. The difference between right and left side is slightly more pronounced with the separate approach. Wall and pedestal surfaces have an equivalent Lambertian reflectance, which is higher than that of the ground surfaces for both approaches. We recall that the spherical target has a reflectance close to 1 and that consequently the results with the surface fitting approach are in fact better with high equivalent Lambertian reflectance: the results are therefore logically less good for the ground.

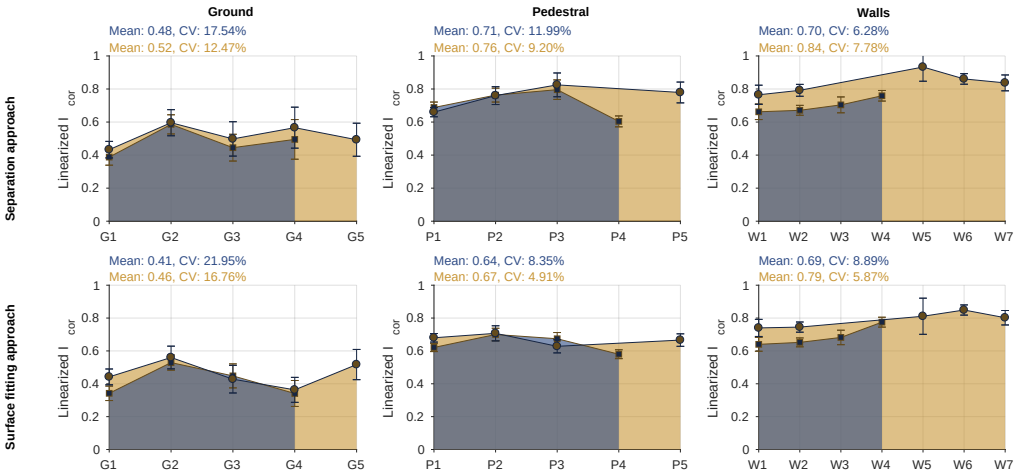

Figure 11: Separation and fitting approaches applied on the two previous heterogeneous 3D clouds. Comparison of linearized corrected intensities for various surfaces, on a [0;1] scale.

5. Conclusion

This paper provides a physical and algorithmic focus on LiDAR TLS intensity measurement, and on the problematic of radiometric correction. We exposed the acquisition processes and the phenomena affecting the obtained signal. We showed that the interpretation of intensity in terms of absolute reflectance, independently of measurement conditions, must be taken with caution.

Most of previous studies focused their correction on a specific part of intensity measurement, or on a limited portion of range measurement. What emerges is that the geometrical parameters, range and incidence angle, are the foremost effects to be removed. No general law could be established due to the variation of measurement behavior between TLS devices, even for identical models. A synthetic presentation was proposed for two groups of correction methods: model-driven and data-driven.

Two data-driven methods were then analyzed and compared to give an overview of advanced correction methodology: a state-of-the art separation approach, and a surface fitting approach with a spherical target that had never been implemented. These two approaches are not limited to a specific distance range or to a specific type of materials.

Experimental results showed that the two exposed approaches provided a corrected intensity (or relative pseudo-reflectance) that was a non-linear increasing function of the reflectance. A linearization method of the corrected intensity was also proposed and applied to both approaches, giving an equivalent Lambertian reflectance. For applications that did not require a precise reflectance value, the obtained pseudo-reflectance may be sufficient.

In addition to providing comparable results to those of the separation approach, the surface fitting approach is more general since it is not established on preconceived assumptions which do not take certain phenomena into account. For example, at short distance, the intensity variation depends strongly on both distance and incidence angle; the correction is then degraded in this case with the separation approach which corrects separately distance and incidence angle (defined at a certain distance). Also, the single regression over the entire intensity versus distance curve hardly fit the not-so-smooth curve shapes.

However, the choice of which method to use will be based predominantly on the requirements and on the available targets. If a geometrically corrected intensity (viewpoint-independant) is only requiered, then the surface fitting approach with a spherical target is better by its practicability and generality. If a full calibrated intensity is required, a Spectralon with calibrated reflectances is needed. In this case a separation approach can be used for already tested scanner models for which the method has already been validated in the literature. A process of linearization of the corrected intensities for calibration is then required. At last, the most efficient calibration process, which would require both Spectralon and spherical targets, is to use the surface fitting approach with spherical target for correction, and a linearization process of the Spectralon corrected intensities for calibration.

6. Acknowledgments

This work was supported by the Agence National de la Recherche (ANR) french institut, Paris, inside the SUMUM project, which aims to improve process and tools for heritage digitization. The authors declare no conflicts of interest.

References

[1] Pesci Arianna and Giordano Teza. Terrestrial laser scanner and retro-reflective targets: An experiment for anomalous effects investigation. *International Journal of Remote Sensing*, 29:5749–5765, 2008.

[2] Julia Armesto-González, Belén Riveiro-Rodríguez, Diego González-Aguilera, and M. Teresa Rivas-Brea. Terrestrial laser scanning intensity data applied to damage detection for historical buildings. *Journal of Archaeological Science*, 37(12):3037 – 3047, 2010.

[3] Mathilde A.F. Balduzzi, Dimitry Van der Zande, Jan Stuckens, Willem W. Verstraeten, and Pol Coppin. The Properties of Terrestrial Laser System Intensity for Measuring Leaf Geometries: A Case Study with Conference Pear Trees (Pyrus Communis). *Sensors*, 11(2):1657–1681, January 2011.

[4] R. Blaskow and D. Schneider. Analysis and correction of the dependency between laser scanner intensity values and range. *ISPRS - International Archives of the Photogrammetry, Remote Sensing and Spatial Information Sciences*, XL-5:107–112, June 2014.

[5] James F. Blinn. Models of light reflection for computer synthesized pictures. *ACM SIGGRAPH Computer Graphics*, 11(2):192–198, August 1977.

[6] Estelle Bretagne, Pascal Dassonvalle, and Guillaume Caron. Spherical target-based calibration of terrestrial laser scanner intensity. Application to colour information computation. *ISPRS Journal of Photogrammetry and Remote Sensing*, 144:14–27, October 2018.

[7] Christian Briese, Martin Pfennigbauer, H Lehner, Andreas Ullrich, W Wagner, and N Pfeifer. Radiometric calibration of multi-wavelength airborne laser scanning data. *ISPRS Ann. Photogramm. Remote Sens. Spat. Inf. Sci*, 1:335–340, 2012.

[8] Dario Carrea, Antonio Abellan, Florian Humair, Battista Matasci, Marc-Henri Derron, and Michel Jaboyedoff. Correction of terrestrial LiDAR intensity channel using Oren–Nayar reflectance model: An application to lithological differentiation. *ISPRS Journal of Photogrammetry and Remote Sensing*, 113:17–29, March 2016.

[9] Franco Coren and Paolo Sterzai. Radiometric correction in laser scanning. *International Journal of Remote Sensing*, 27(15):3097–3104, August 2006.

[10] Nathan Crombez, Guillaume Caron, and E Mouaddib. 3d point cloud model colorization by dense registration of digital images. *The International Archives of Photogrammetry, Remote Sensing and Spatial Information Sciences*, 40(5):123, 2015.

[11] Qiong Ding, Wu Chen, Bruce King, Yanxiong Liu, and Guoxiang Liu. Combination of overlap-driven adjustment and Phong model for LiDAR intensity correction. *ISPRS Journal of Photogrammetry and Remote Sensing*, 75:40–47, January 2013.

[12] Pinliang Dong and Qi Chen. *LiDAR remote sensing and applications*. Remote sensing applications series. CRC Press, Taylor & Francis, Boca Raton London New York, 2018. OCLC: 1019706410.

[13] Jan U.H. Eitel, Bernhard Höfle, Lee A. Vierling, Antonio Abellán, Gregory P. Asner, Jeffrey S. Deems, Craig L. Glennie, Philip C. Joerg, Adam L. LeWinter, Troy S. Magney, Gottfried Mandlburger, Douglas C. Morton, Jörg Müller, and Kerri T. Vierling. Beyond 3-D: The new spectrum of lidar applications for earth and ecological sciences. *Remote Sensing of Environment*, 186:372–392, December 2016.

[14] Angus Errington and Brian Daku. Temperature Compensation for Radiometric Correction of Terrestrial LiDAR Intensity Data. *Remote Sensing*, 9(4):356, April 2017.

[15] Angus FC Errington, Brian LF Daku, and Arnfinn F Prugger. Reflectance modelling using terrestrial lidar intensity data. In *2015 IEEE International Conference on Imaging Systems and Techniques (IST)*, pages 1–6. IEEE, 2015.

[16] Angus FC Errington, Brian LF Daku, and Arnfinn F Prugger. Clay mapping in underground potash mines: An initial investigation into the use of corrected intensity terrestrial lidar data. In *2016 IEEE International Conference on Imaging Systems and Techniques (IST)*, pages 94–99, 2016.

[17] Wei Fang, Xianfeng Huang, Fan Zhang, and Deren Li. Intensity correction of terrestrial laser scanning data by estimating laser transmission function. *IEEE Transactions on Geoscience and Remote Sensing*, 53(2):942–951, 2014.

[18] Alireza G. Kashani, Michael Olsen, and Andrew Graettinger. Laser scanning intensity analysis for automated building wind damage detection. *Congress on Computing in Civil Engineering, Proceedings*, 2015, 06 2015.

[19] Guy Godin, Marc Rioux, Marc Levoy, Luc Cournoyer, and François Blais. An assessment of laser range measurement on marble surfaces. 2001.

[20] Bernhard Höfle and Norbert Pfeifer. Correction of laser scanning intensity data: Data and model-driven approaches. *ISPRS Journal of Photogrammetry and Remote Sensing*, 62(6):415–433, December 2007.

[21] A Jaakkola, S Kaasalainen, J Hyyppä, A Akujärvi, and H Niittymäki. Radiometric calibration of intensity images of swissranger sr-3000 range camera. *Photogramm. J. Finland*, 21(1):16–25, 2008.

[22] A.V. Jelalian. Laser radar systems. *Artech House, Boston London*, 1992.

[23] Junling Jin, Lars De Sloover, Jeffrey Verbeurgt, Cornelis Stal, Greet Deruyter, Anne-Lise Montreuil, Philippe De Maeyer, and Alain De Wulf. Measuring surface moisture on a sandy beach based on corrected intensity data of a mobile terrestrial lidar. *Remote Sensing*, 12(2):209, 2020.

[24] Boris Jutzi and H Gross. Normalization of lidar intensity data based on range and surface incidence angle. *Int. Arch. Photogramm. Remote Sens. Spat. Inf. Sci*, 38:213–218, 2009.

[25] Boris Jutzi and Hermann Gross. Investigations on surface reflection models for intensity normalization in airborne laser scanning (als) data. *Photogrammetric Engineering & Remote Sensing*, 76(9):1051–1060, 2010.

[26] Sanna Kaasalainen, Hannu Hyyppa, Antero Kukko, Paula Litkey, Eero Ahokas, Juha Hyyppa, Hubert Lehner, Anttoni Jaakkola, Juha Suomalainen, Altti Akujarvi, et al. Radiometric calibration of lidar intensity with commercially available reference targets. *IEEE Transactions on Geoscience and Remote Sensing*, 47(2):588–598, 2008.

[27] Sanna Kaasalainen, Anttoni Jaakkola, Mikko Kaasalainen, Anssi Krooks, and Antero Kukko. Analysis of incidence angle and distance effects on terrestrial laser scanner intensity: Search for correction methods. *Remote Sensing*, 3(10):2207–2221, 2011.

[28] Sanna Kaasalainen, Harri Kaartinen, and Antero Kukko. Snow cover change detection with laser scanning range and brightness measurements. *EARSeL eProc*, 7(2):133–141, 2008.

[29] Sanna Kaasalainen, Anssi Krooks, Antero Kukko, and Harri Kaartinen. Radiometric Calibration

of Terrestrial Laser Scanners with External Reference Targets. *Remote Sensing*, 1(3):144–158, July 2009.

[30] Sanna Kaasalainen, Antero Kukko, Tomi Lindroos, Paula Litkey, Harri Kaartinen, Juha Hyyppa, and Eero Ahokas. Brightness measurements and calibration with airborne and terrestrial laser scanners. *IEEE transactions on geoscience and remote sensing*, 46(2):528–534, 2008.

[31] Sanna Kaasalainen, Ants Vain, Anssi Krooks, and Antero Kukko. Topographic and distance effects in laser scanner intensity correction. 2009.

[32] Alireza G Kashani, Michael J Olsen, Christopher E Parrish, and Nicholas Wilson. A review of lidar radiometric processing: From ad hoc intensity correction to rigorous radiometric calibration. *Sensors*, 15(11):28099–28128, 2015.

[33] A Krooks, S Kaasalainen, T Hakala, and O Nevalainen. Correction of intensity incidence angle effect in terrestrial laser scanning. *ISPRS Ann. Photogramm. Remote Sens. Spat. Inf. Sci*, 2:145–150, 2013.

[34] Antero Kukko, Sanna Kaasalainen, and Paula Litkey. Effect of incidence angle on laser scanner intensity and surface data. *Applied Optics*, 47(7):986–992, 2008.

[35] Fred Edwin Nicodemus, NICODEMUS FE, and RICHMOND JC. Geometrical considerations and nomenclature for reflectance. Technical report, 1977.

[36] Michael Oren and Shree K Nayar. Generalization of lambert's reflectance model. In *Proceedings of the 21st annual conference on Computer graphics and interactive techniques*, pages 239–246, 1994.

[37] Norbert Pfeifer, Peter Dorninger, Alexander Haring, and Hongchao Fan. Investigating terrestrial laser scanning intensity data: quality and functional relations. 2007.

[38] Norbert Pfeifer, Bernhard Höfle, Christian Briese, Martin Rutzinger, and Alexander Haring. Analysis of the backscattered energy in terrestrial laser scanning data. *Int. Arch. Photogramm. Remote Sens. Spat. Inf. Sci*, 37:1045–1052, 2008.

[39] Martin Pfennigbauer and Andreas Ullrich. Improving quality of laser scanning data acquisition through calibrated amplitude and pulse deviation measurement. page 76841F, Orlando, Florida, April 2010.

[40] Bui Tuong Phong. Illumination for computer generated pictures. *Communications of the ACM*, 18(6):311–317, June 1975.

[41] Richard D Richmond, Stephen C Cain, and Society of Photo-optical Instrumentation Engineers. *Direct-detection LADAR systems*. SPIE, Bellingham, Wash., 2010. OCLC: 726831190.

[42] M Scaioni, B Höfle, AP Baungarten Kersting, L Barazzetti, M Previtali, D Wujanz, et al. Methods from information extraction from lidar intensity data and multispectral lidar technology. In *2018 ISPRS TC III Mid-Term Symposium on Developments, Technologies and Applications in Remote Sensing*, volume 42, pages 1503–1510. International Society for Photogrammetry and Remote Sensing, 2018.

[43] Jeffrey H. Shapiro. Target-reflectivity theory for coherent laser radars. *Applied Optics*, 21(18):3398, September 1982.

[44] Ove Steinvall. Effects of target shape and reflection on laser radar cross sections. *Applied Optics*, 39(24):4381, August 2000.

[45] Kai Tan and Xiaojun Cheng. Intensity data correction based on incidence angle and distance for terrestrial laser scanner. *Journal of Applied Remote Sensing*, 9(1):094094, September 2015.

[46] Kai Tan and Xiaojun Cheng. Surface reflectance retrieval from the intensity data of a terrestrial laser scanner. *Journal of the Optical Society of America A*, 33(4):771, April 2016.

[47] Kai Tan, Xiaojun Cheng, Xiaoli Ding, and Qi Zhang. Intensity Data Correction for the Distance Effect in Terrestrial Laser Scanners. *IEEE Journal of Selected Topics in Applied Earth Observations and Remote Sensing*, 9(1):304–312, January 2016.

[48] Tee-Ann Teo and Hui-Lin Yu. Empirical Radiometric Normalization of Road Points from Terrestrial Mobile Lidar System. *Remote Sensing*, 7(5):6336–6357, May 2015.

[49] K. E. Torrance and E. M. Sparrow. Theory for Off-Specular Reflection From Roughened Surfaces*. *Journal of the Optical Society of America*, 57(9):1105, September 1967.

[50] Ants Vain, Sanna Kaasalainen, Ulla Pyysalo, Anssi Krooks, and Paula Litkey. Use of Naturally Available Reference Targets to Calibrate Airborne Laser Scanning Intensity Data. *Sensors*, 9(4):2780–2796, April 2009.

[51] Wolfgang Wagner. Radiometric calibration of small-footprint full-waveform airborne laser scanner measurements: Basic physical concepts. *ISPRS Journal of Photogrammetry and Remote Sensing*, 65(6):505–513, 2010.

[52] J. Wojtanowski, M. Zygmunt, M. Kaszczuk, Z. Mierczyk, and M. Muzal. Comparison of 905 nm and 1550 nm semiconductor laser rangefinders' performance deterioration due to adverse environmental

conditions. *Opto-Electronics Review*, 22(3), January 2014.

[53] Teng Xu, Lijun Xu, Bingwei Yang, Xiaolu Li, and Junen Yao. Terrestrial Laser Scanning Intensity Correction by Piecewise Fitting and Overlap-Driven Adjustment. *Remote Sensing*, 9(11):1090, October 2017.

Appendix

			Uncorrected		Separation approach		Surface fitting approach	
			I_{raw} $(R, \alpha<15°)$	I_{raw} $(\alpha, R=10m)$	I_{cor} $(R, \alpha<15°)$	I_{cor} $(\alpha, R=10m)$	I_{cor} $(R, \alpha<15°)$	I_{cor} $(\alpha, R=10m)$
Sphere dataset		mean	0.82	0.82	0.81	0.81	0.86	0.87
		std	0.042	0.041	0.007	0.002	0.003	0.002
		CV	5.19	5.05	0.91	0.25	0.45	0.31
Spectralon dataset	99%	mean	0.85	0.82	0.84	0.82	0.89	0.87
		std	0.035	0.060	0.010	0.008	0.009	0.008
		CV	4.09	7.29	1.24	0.97	1.07	0.92
	57%	mean	0.79	0.77	0.78	0.77	0.83	0.82
		std	0.036	0.054	0.006	0.006	0.005	0.006
		CV	4.64	7.01	0.81	0.89	0.62	0.81
	28%	mean	0.72	0.71	0.71	0.71	0.75	0.76
		std	0.040	0.045	0.006	0.002	0.006	0.003
		CV	5.53	6.35	0.85	0.37	0.82	0.42
	11%	mean	0.60	0.61	0.59	0.61	0.63	0.65
		std	0.043	0.028	0.012	0.014	0.013	0.016
		CV	7.14	4.72	2.12	2.40	2.18	2.52

Table 7: Quantitative comparison of Separation and Surface fitting approaches with raw intensities on sphere and Spectralon datasets.

					Uncorrected		Separation approach		Surface fitting approach	
			R (m)	α (°)	mean	std	mean	std	mean	std
Left side	Ground	G1	2.68	59.48	0.71	0.013	0.73	0.014	0.77	0.017
		G2	7.99	80.57	0.71	0.016	0.78	0.010	0.82	0.010
		G3	15.22	84.87	0.57	0.013	0.75	0.017	0.80	0.019
		G4	23.86	86.68	0.58	0.018	0.76	0.023	0.77	0.025
	Pedestal	P1	3.06	50.69	0.80	0.006	0.79	0.005	0.84	0.005
		P2	3.54	78.13	0.72	0.005	0.81	0.005	0.86	0.007
		P3	3.05	75.92	0.72	0.008	0.81	0.008	0.85	0.007
		P4	3.53	72.75	0.72	0.005	0.78	0.005	0.83	0.006
	Walls	W1	35.68	24.42	0.77	0.008	0.79	0.007	0.85	0.008
		W2	32.63	8.39	0.79	0.005	0.79	0.004	0.85	0.005
		W3	36.26	27.05	0.78	0.007	0.80	0.007	0.85	0.008
		W4	33.39	37.47	0.78	0.005	0.80	0.004	0.87	0.005
Right side	Ground	G1	3.80	69.16	0.71	0.012	0.75	0.012	0.80	0.013
		G2	9.41	81.77	0.68	0.020	0.78	0.013	0.83	0.015
		G3	18.41	85.81	0.57	0.016	0.76	0.021	0.80	0.023
		G4	25.07	86.67	0.59	0.018	0.77	0.023	0.78	0.023
		G5	12.80	84.01	0.60	0.018	0.76	0.019	0.82	0.020
	Pedestal	P1	4.29	39.18	0.84	0.005	0.79	0.004	0.85	0.005
		P2	4.24	79.98	0.72	0.007	0.80	0.007	0.86	0.008
		P3	5.04	81.66	0.74	0.009	0.81	0.009	0.84	0.008
		P5	5.04	71.42	0.79	0.009	0.81	0.009	0.85	0.007
	Walls	W1	37.13	24.16	0.79	0.008	0.80	0.008	0.86	0.009
		W2	34.25	11.13	0.80	0.005	0.81	0.004	0.86	0.005
		W5	30.12	72.77	0.71	0.016	0.83	0.019	0.88	0.020
		W6	21.59	45.09	0.77	0.004	0.82	0.004	0.88	0.005
		W7	19.40	52.11	0.75	0.006	0.81	0.006	0.87	0.007

Table 8: Mean and standard deviation of selected area intensities on an heterogeneous point cloud before and after correction.